Optical Materials 48 (2015) 150–155

Contents lists available at ScienceDirect

Optical Materials

journal homepage: www.elsevier.com/locate/optmat

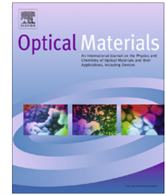

Integration of silicon-loaded nanoplasmonic waveguides onto a micro-machined characterization beam for nonlinear optics applications

S. Sederberg [1], A.Y. Elezzabi *

Ultrafast Optics and Nanophotonics Research Laboratory, Department of Electrical and Computer Engineering, University of Alberta, Edmonton T6G 2V4, Canada

ARTICLE INFO

Article history:
Received 19 May 2015
Received in revised form 25 July 2015
Accepted 27 July 2015

Keywords:
Nanoplasmonics
Integrated optics
Ultrafast optics
Nanofabrication

ABSTRACT

Silicon-loaded nanoplasmonic waveguides were integrated onto a micron-scale characterization beam to allow for accurate and efficient nonlinear optical characterization. The waveguides consist of a 95 nm × 340 nm silicon core that is capped by a 60 nm thick gold film. The characterization beam is formed by precision cleaving one waveguide end facet and by deep silicon etching the substrate area adjacent to the other end facet. This configuration allows input radiation to be coupled directly to the waveguides using a microscope objective and output radiation to be out-coupled with a lensed single-mode optical fiber. The fabrication steps are characterized via scanning electron microscopy at various points throughout the process. The fabricated devices are optically characterized using an ultrafast nonlinear pump–probe time-domain spectroscopy setup. Ultrafast all-optical modulation is measured in the waveguides on two timescales: $\tau_1 = 1.98 \pm 0.40$ ps and $\tau_2 = 17.9 \pm 6.8$ ps.

© 2015 Elsevier B.V. All rights reserved.

1. Introduction

Fiber optical networks have proven to outperform electrical networks in bandwidth and energy consumption. This success has motivated substantial effort into developing chip-scale photonic waveguide circuits. Silicon (Si) photonic devices fabricated on silicon-on-insulator (SOI) substrates have reached a sophisticated level of development and their integration with complementary metal–oxide–semiconductor devices is undergoing rapid development. As such, optical interconnects have been proposed as a means to alleviate resistive–capacitive delays in the present electrical scheme [1]. While photonic waveguides show promising applications, their minimum cross-sectional dimensions are limited by the light wave diffraction limit. However, for high integration density applications when the separation between waveguides is reduced to the order of a wavelength, photonic waveguides exhibit prohibitive cross-talk due to mode coupling. Furthermore, sharp bends in photonic waveguides result in radiation losses of the propagating optical mode. All of these factors limit the maximum integration density achievable with photonic waveguides.

Plasmonic waveguides function in a similar manner as photonic waveguides, but incorporate low-loss metal (Au, Ag, Al, and Cu) features. When an appropriate coupling scheme is used, free-space radiation can excite an electromagnetic mode at the interface between metallic features and adjacent dielectric materials. The incident radiation couples strongly to the conduction electrons of the metal and the mode propagates as a coupled oscillation of charge density in the metal and evanescent electromagnetic fields in the dielectric. The strong coupling of radiation to the metal features has enabled demonstration of waveguide devices with cross-sectional dimensions as small as a few tens of nanometers [2]. Plasmonic waveguides also exhibit low cross talk and low bending losses compared to their photonic counterparts.

Along with the aforementioned characteristics, this strong confinement produces an enhancement in the amplitude of the electric field in the vicinity of the metal features. In the case of a nanoplasmonic waveguide, fields can be enhanced by several times their original strength. The enhanced fields can be used to magnify light-matter interaction processes, such as chemical detection [3] or nonlinear optical processes [4,5]. While plasmonic waveguides have several attractive characteristics, strong interaction of the radiation with metals results in propagation losses that are higher than photonic waveguides. The characteristic propagation length of electromagnetic energy in a subwavelength plasmonic waveguide depends strongly on the materials and design of the waveguide and may range from several microns to several tens of

* Corresponding author.
E-mail addresses: shawn.sederberg@mpq.mpg.de (S. Sederberg), elezzabi@ece.ualberta.ca (A.Y. Elezzabi).

[1] Present address: Max-Planck-Institute of Quantum Optics, Hans-Kopfermann-Strasse 1, 85748 Garching, Germany.

http://dx.doi.org/10.1016/j.optmat.2015.07.036
0925-3467/© 2015 Elsevier B.V. All rights reserved.

microns. Long-range surface plasmon polariton waveguides have dimensions larger than the optical wavelength, but enable light propagation over millimeter length scales [6,7].

Coupling radiation into nanoplasmonic waveguides with micron-scale lengths requires a carefully designed on-chip coupler, which may add additional fabrication complexities [8,9]. Previous coupling schemes have incorporated prisms [10], photonic bus waveguides [11], gratings [12], plasmonic antennas [13], and nano-mirrors [14] to direct the free-space radiation to the nanoplasmonic waveguide mode.

However, a key predicament in accessing ultrafast active operation in a Si-nanoplasmonic waveguide device is the ability to couple the optical signal directly into the device. That is, when considering nonlinear optical interaction effects in Si-based nanoplasmonic waveguides, it is not possible to achieve efficient nonlinear interaction in the plasmonic region, as nonlinear interaction can occur within the on-chip coupler. End-fire coupling radiation directly into the nanoplasmonic waveguide would eliminate the need for a coupler, but requires separation of the substrate into micron-scale die, which would make subsequent handling and characterization prohibitively challenging. Moreover, these dimensional constraints push traditional die separation techniques, such as dicing or scribing beyond their prescribed abilities. Therefore, it would be beneficial to develop a means to integrate nanoplasmonic waveguides with lengths of several microns onto a macroscopic die in a configuration that would allow their end-facets to be directly accessed with macroscopic objects such as microscope objectives and optical fibers. Realization of such a sample would enable efficient access to nonlinear optical effects and ultrafast modulation in Si-loaded nanoplasmonic waveguides.

In this work, we fabricate Si-loaded nanoplasmonic waveguides and integrate these structures onto a micron-scale "characterization beam." This characterization beam allows for direct coupling to the waveguides using microscope objectives and optical fibers and enables accurate measurements of ultrafast nonlinear interactions taking place in the waveguide.

2. Device design

The waveguide geometry consists of a Si waveguide core with cross-sectional dimensions, $w \times h = 95\ \text{nm} \times 340\ \text{nm}$. The Si core is capped by a gold (Au) film of a thickness, $t = 60\ \text{nm}$. The cross-sectional geometry of the waveguide is depicted schematically in Fig. 1(a) and the corresponding nanoplasmonic mode profile was obtained with an electromagnetic mode solver and is shown in Fig. 1(b). The theoretical distance propagated by the mode before attenuating to e^{-1} of its initial amplitude was found to be $L_{prop} = 3.1\ \mu\text{m}$. In order to ensure a strong signal is transmitted through the device, we consider waveguides with lengths, $L \leqslant 10\ \mu\text{m}$.

A schematic depiction of several nanoplasmonic waveguides integrated onto the characterization beam is shown in Fig. 1(c). In this design, the width of the characterization beam is increased in steps, allowing the waveguide length to be varied. As labeled in Fig. 1(c), one face of the characterization beam is defined by cleaving the SOI wafer and the other is defined by deep etching the Si handle wafer. A deeply etched line is used to define the cleavage plane, ensuring that the cleave intersects the waveguide end-facets. The implementation of this technique is discussed further in Section 4. Notably, a cleaved facet allows for a bulky microscope objective to be brought in close proximity to the sample for excitation. We consider etching depths, $d_{etch} = 75\ \mu\text{m}$, allowing for an optical fiber to be brought over the substrate to the output facet of the waveguide. The proposed excitation and detection scheme is depicted schematically in Fig. 1(c).

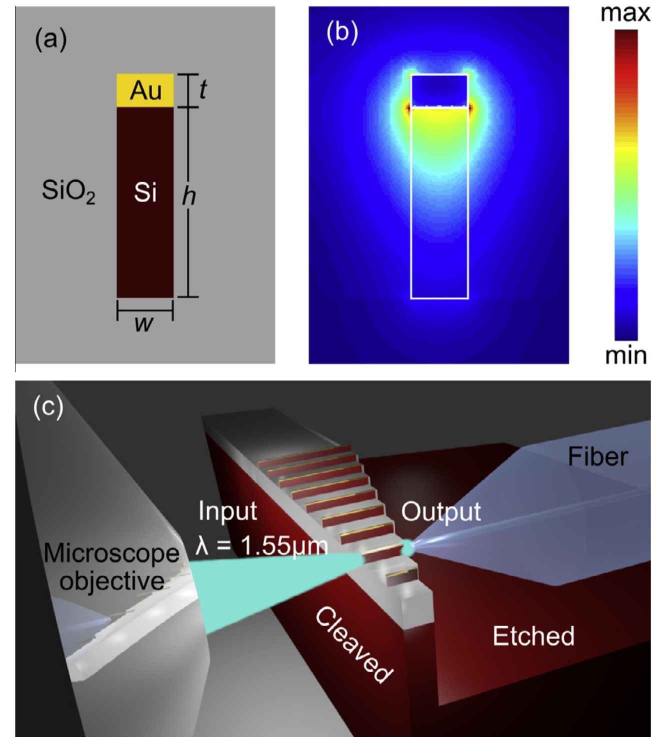

Fig. 1. (a) Schematic of the cross-sectional geometry of the nanoplasmonic waveguide. (b) Distribution of electric field amplitude in the nanoplasmonic waveguide. (c) Schematic of nanoplasmonic waveguides integrated onto a characterization beam, along with the microscope excitation and optical fiber detection configuration.

3. Nanofabrication

3.1. Nanoplasmonic waveguide definition

In order to maintain compatibility with Si photonic devices, we used a SOI substrate with a device layer thickness, $t_{dev} = 340\ \text{nm}$, a buried oxide layer thickness, $t_{BOX} = 1\ \mu\text{m}$, and an overall substrate thickness, $t_{sub} = 500\ \mu\text{m}$. The fabrication process involved two layers of electron beam lithography (EBL), which were performed using a Raith 150-TWO system.

Organic contamination was removed from the sample by placing it in an ultrasonic bath of acetone for 10 min, followed by a 15 min immersion in Piranha solution (3:1 mixture of 96% H_2SO_4 to 30% H_2O_2). The native oxide was removed by a 45 s bath in buffered hydrofluoric acid (1 HF:10 NH_4F). A schematic depiction of the bare SOI substrate is shown in Fig. 2(a).

In preparation for the first layer of EBL, a layer of 6% 495 K poly(methyl methacrylate) in anisole (495 k PMMA A6) was spun onto the substrate at 5000 rpm (RPM), producing a resist thickness of $t_{PMMA,1} = 275\ \text{nm}$. The sample was then baked at 180 °C for 15 min. The pattern was exposed using an aperture diameter, $d = 20\ \mu\text{m}$, an acceleration voltage, $V = 20\ \text{keV}$, and an area dosage, $D = 450\ \mu\text{C/cm}^2$. The sample was developed in a methylisobutylketone (MIBK)-based developer (1 MIBK:3 isopropyl alcohol (IPA)) for 45 s. Four subsequent thin films were deposited on the sample using an electron beam evaporation system. The first layer was a $t_{Cr,1} = 5\ \text{nm}$ chromium (Cr) adhesion layer. The second was a $t_{Au} = 60\ \text{nm}$ Au layer, which gives the waveguide its ability to guide optical signals at sub-diffraction dimensions. The third was an additional $t_{Cr,2} = 5\ \text{nm}$ Cr adhesion layer, and the final layer was a $t_{SiO_2,1} = 40\ \text{nm}$ SiO_2 layer, which acted as an etch mask to prevent sputtering of the soft Au features during subsequent plasma

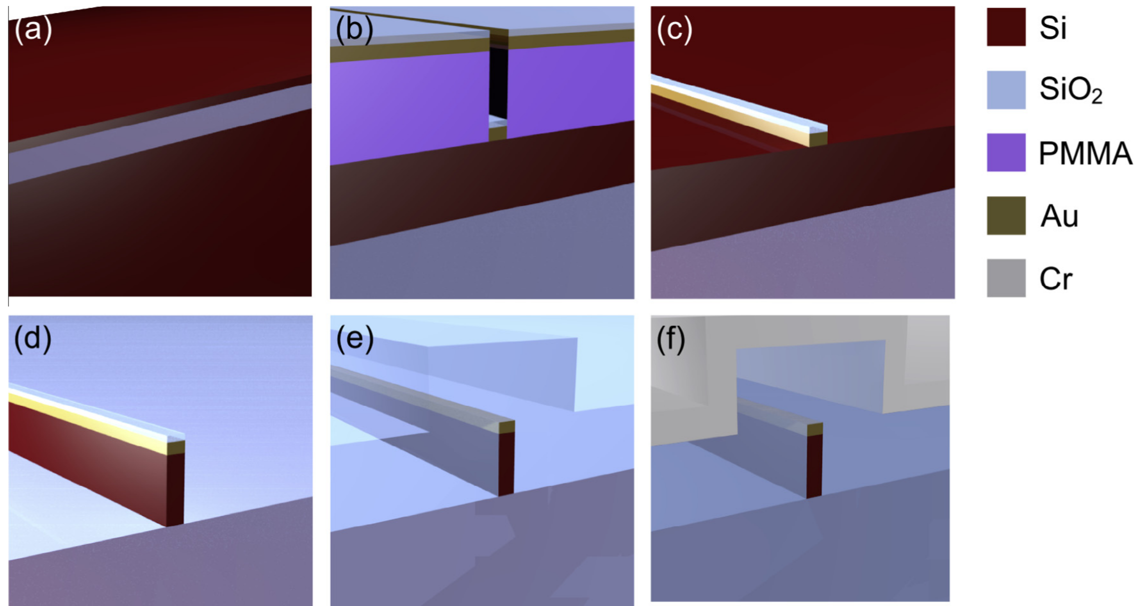

Fig. 2. (a) Silicon-on-insulator substrate. (b) First EBL exposure, followed by electron beam evaporation of Cr(5 nm) + Au(60 nm) + Cr(5 nm) + SiO_2(40 nm). (c) Evaporated films after lift-off. (d) A fully-defined nanoplasmonic waveguide after ICPRIE etching through the Si device layer. (e) A nanoplasmonic waveguide embedded in a 500 nm thick SiO_2 cladding. (f) Subsequent deposition of 150 nm thick chromium etch mask.

processing. The EBL pattern along with the deposited films is shown schematically in Fig. 2(b). After deposition, a standard lift-off in an ultrasonic bath of acetone was performed, and the sample was cleaned in this manner for 20 min. A nanoplasmonic waveguide after the lift-off step is shown in Fig. 2(c).

The pattern was transferred through the Si device layer using an unswitched recipe in an inductively coupled plasma reactive ion etching (ICPRIE) system, shown in Fig. 2(d). In order to avoid scalloping in the waveguide sidewalls that would be produced by the Bosch process [15], we expose the sample to C_4F_8 (80 sccm), SF_6 (85 sccm), and O_2 (5 sccm) simultaneously. This produces a continuous etch with smooth sidewalls, minimizing scattering losses of the nanoplasmonic mode. It has previously been demonstrated that metallic masks can lead to substantial undercut in the etching profile [16]. Although the Au features were capped by a SiO_2 etch mask, it was found that even etching in close proximity to Au features produced substantial undercut, and it was necessary to increase the C_4F_8 passivation gas flow from 40 sccm (which was optimal for a PMMA mask) to 80 sccm.

Next, we deposited a $t_{SiO_2,2} = 500$ nm layer of SiO_2 using plasma-enhanced chemical vapor deposition (PECVD), which served several purposes. Primarily, it acted as a waveguide cladding, giving the waveguide a uniform refractive index environment. In addition, it protected the waveguides during subsequent processing steps and from their environment during optical characterization. The SiO_2-clad waveguide is shown in Fig. 2(e). A Cr layer with a thickness of $t_{Cr,3} = 150$ nm was deposited on the sample via magnetron sputtering, as shown in Fig. 2(f), and was used to define an etch mask.

Scanning electron micrographs (SEMs) of typical results taken during several steps of the fabrication are shown in Fig. 3. Fig. 3(a) shows a top-view SEM of a typical Cr–Au–Cr–SiO_2 waveguide cap after completing the lift-off step. A tilted-view SEM showing the nanoplasmonic waveguide sidewall quality after dry etching through the Si device layer is shown in Fig. 3(b). An SEM of a nanoplasmonic waveguide buried beneath the SiO_2 cladding and the Cr etch mask is shown in Fig. 3(c) and is depicted schematically in Fig. 4(a).

3.2. Characterization beam definition

The next layer of lithography involves micron-scale features that must be aligned to the existing features with a misalignment tolerance of $\delta < 100$ nm. Therefore, we exposed the pattern via EBL, which employed laser interferometry to position the sample stage and enabled overlay alignment accuracy on the order of a few tens of nanometers. In preparation for the second layer of EBL, a $t_{PMMA,2} = 275$ nm layer of 495 K PMMA A6 was spun onto the sample and baked for 15 min at 180 °C. In order to reduce the exposure time, we used a large electron beam aperture diameter, $d = 120$ μm, an acceleration voltage, $V = 20$ keV, and an area dose of $D = 200$ μC/cm^2. The fixed beam moving stage feature of the Raith system was used to ensure stitch-free exposure between write fields [17]. The sample was developed in 1 MIBK:3 IPA developer for 45 s.

The pattern was transferred through the Cr layer using a commercially available solution of ceric ammonium nitrate ($(NH_4)_2Ce(NO_3)_6$), nitric acid (HNO_3), and water (H_2O) and the sample was cleaned in an ultrasonic bath for 20 min. Fig. 4(b) shows a schematic of the Cr mask, which consists of a guide for the cleave plane adjacent to one waveguide end facet and a large cleared area adjacent to the other end facet. The Cr mask was then used to etch through the oxide layer ($t_{SiO_2,2} = 500$ nm PECVD oxide and $t_{BOX} = 1000$ nm thermal oxide), via reactive ion etching (RIE), and to a depth of $d_{etch} = 75$ μm into the Si wafer using the Bosch process in an ICPRIE system. A schematic view of the sample after Bosch etching is shown in Fig. 4(c). At this point, the Cr mask was removed and the sample was cleaved and cleaned in an ultrasonic bath for 20 min.

Fig. 5 depicts typical fabrication results during the definition of the characterization beam and of the final structures. An SEM of the Cr etch mask is shown in Fig. 5(a). The final sample after deep etching and cleaving is shown in Fig. 5(b)–(c). Approximately 10 waveguides are integrated onto the characterization beam, with lengths in the range of 2 μm $\leqslant L \leqslant$ 10 μm. A cross-sectional SEM of the nanoplasmonic waveguide geometry is shown in Fig. 5(d). Close inspection of this image reveals that a remnant of the SiO_2 mask is present on top of the Au cap.

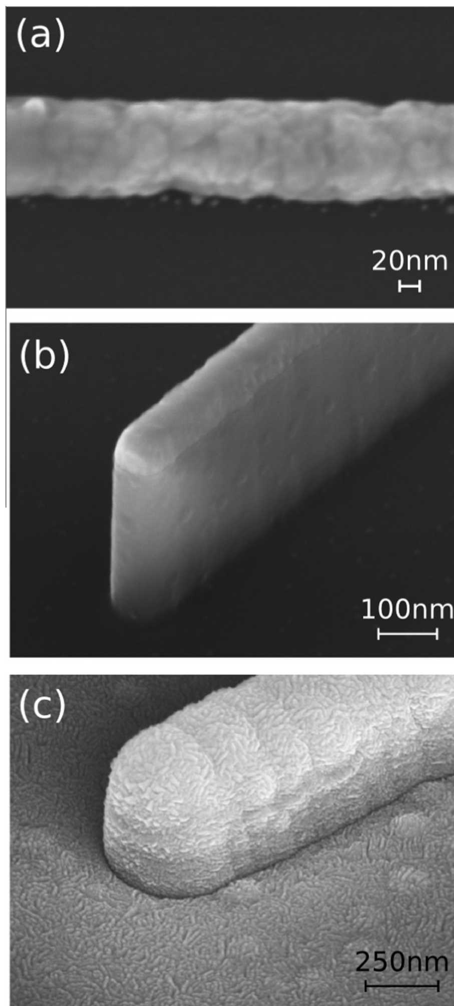

Fig. 3. (a) Top-view SEM of the evaporated films after lift-off. (b) Tilted SEM of the fully defined nanoplasmonic waveguide after etching through the Si device layer. (c) Tilted SEM of a nanoplasmonic waveguide enclosed in a 500 nm SiO_2 cladding and a 150 nm Cr etch mask.

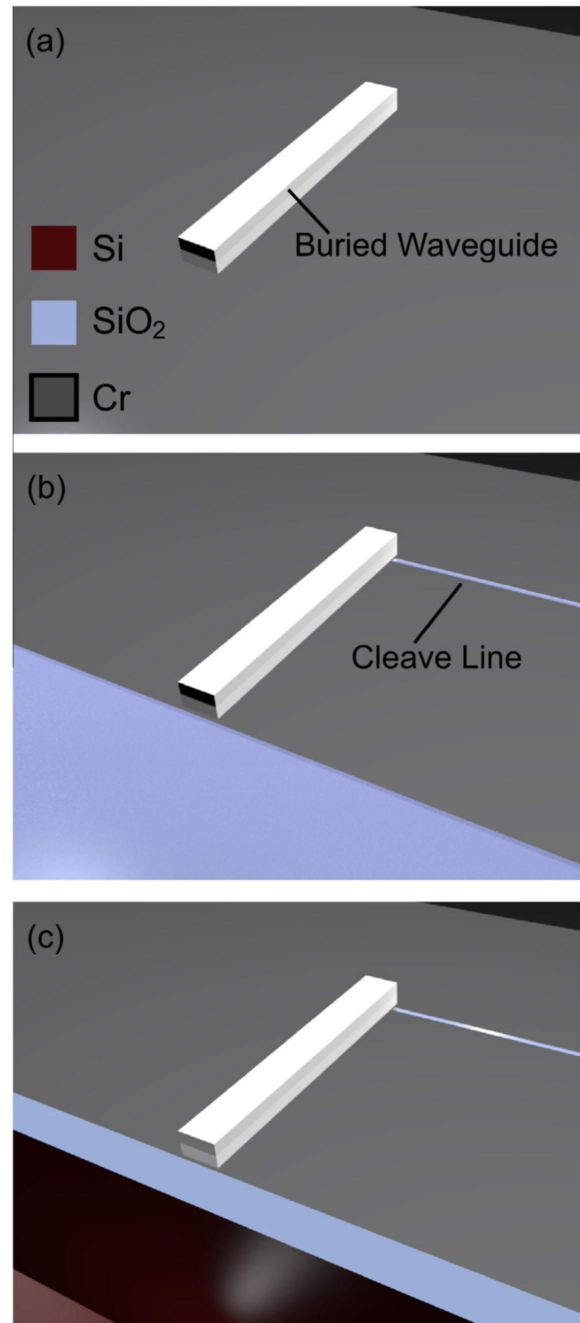

Fig. 4. (a) Schematic of a nanoplasmonic waveguide buried beneath a 500 nm SiO_2 cladding and a 150 nm Cr etch mask. (b) The Cr etch mask consisting of a cleave guide adjacent to one waveguide end facet and a large area adjacent to the other end facet. (c) The sample after etching through the BOX layer and 75 μm into the Si substrate.

4. Optical measurements

4.1. Characterization setup

Following their successful fabrication, nonlinear optical interactions were investigated in the nanoplasmonic waveguides. Strong nonlinear loss mechanisms exist in the silicon core of the nanoplasmonic waveguide, including two-photon absorption (TPA) and free-carrier absorption (FCA) [18]. The nonlinear loss may be used to operate the waveguide as an ultrafast modulator. To visualize the ultrafast temporal dynamics of nonlinear loss in the nanoplasmonic waveguide, we set up a pump–probe characterization system.

An erbium-doped fiber laser that emits pulses with a duration, τ_p = 84 fs, centered at $\lambda = 1550$ nm was used to measure ultrafast nonlinear dynamics in the nanoplasmonic waveguides. The laser pulses were split into a pump and a probe, which had orthogonal polarizations. The probe pulses underwent a variable delay, whereas the pump pulses underwent a fixed delay. The two beams were recombined and coupled into the nanoplasmonic waveguides using a microscope objective (50×, NA = 0.85). The transmitted optical signal was out-coupled using a lensed single mode optical fiber, which delivered the signal to a fast-photodiode and lock-in detection setup. By varying the delay between the pump and probe in a continuous manner, ultrafast nonlinear effects occurring in the nanoplasmonic waveguides were visualized. A schematic of the characterization setup is shown in Fig. 6(a).

4.2. Results

Using the fabrication processes presented earlier, it was also possible to fabricate nanoplasmonic and photonic waveguides side-by-side on the same sample enabling a direct comparison of

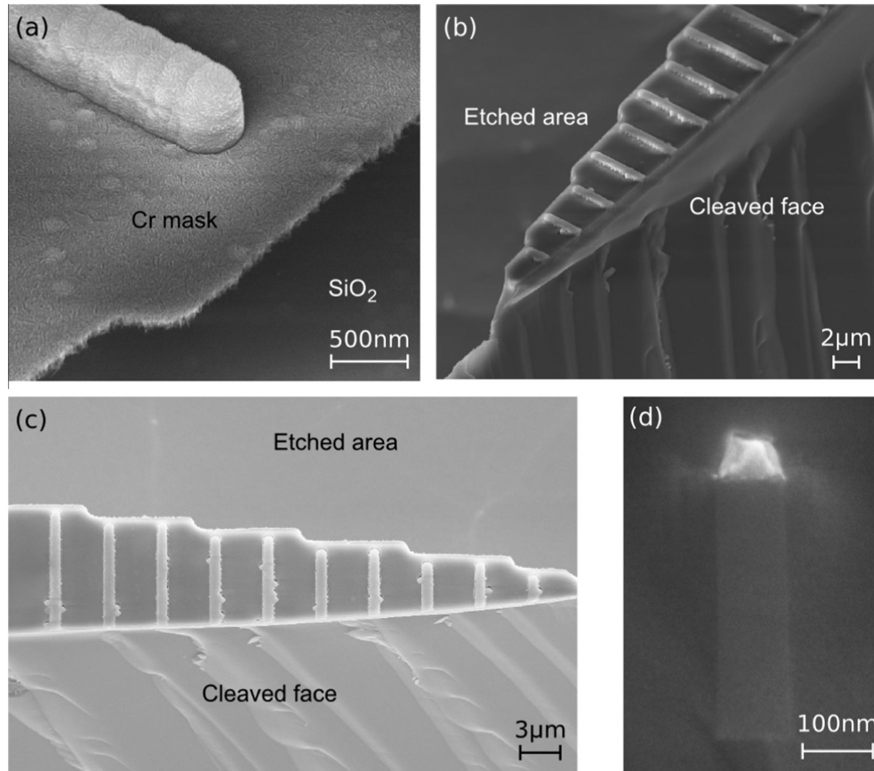

Fig. 5. (a) Tilted SEM of the Cr etch mask adjacent to a nanoplasmonic waveguide. (b) Tilted SEM of the final structure after deep etching and cleaving. (c) Top-view SEM of the final structure after deep etching and cleaving. (d) Cross-sectional SEM of a nanoplasmonic waveguide end facet. A thin remnant of the SiO_2 etch mask is visible on top of the Au cap.

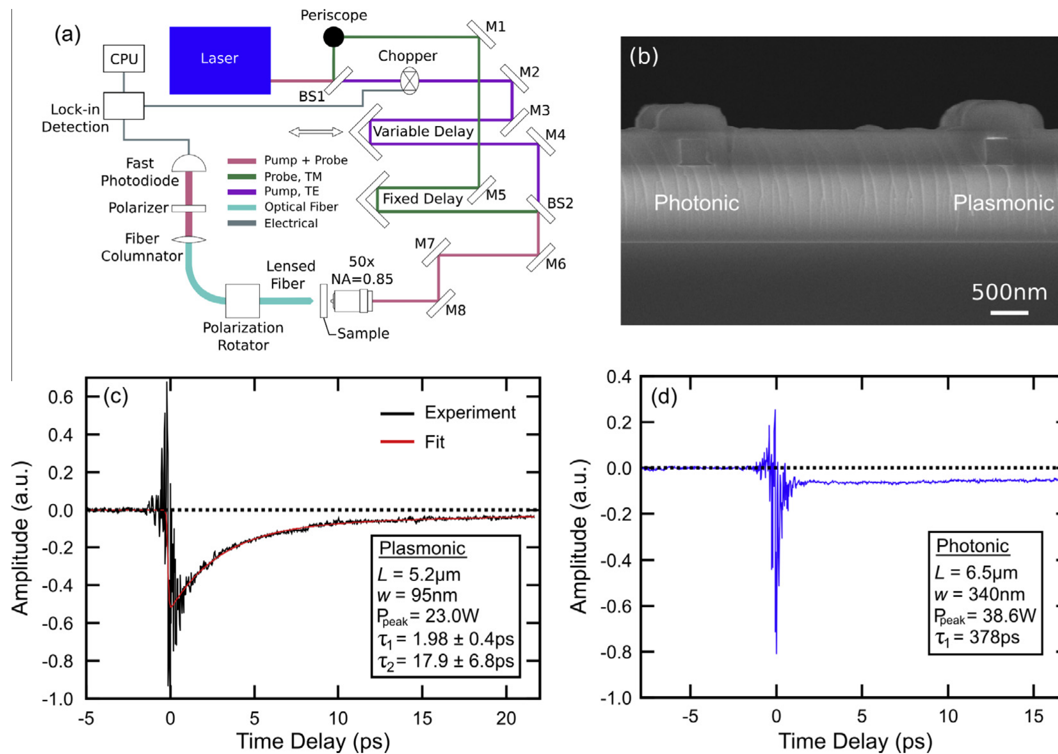

Fig. 6. (a) Schematic of the ultrafast pump–probe characterization setup. (b) SEM of nanoplasmonic and photonic waveguides fabricated side-by-side on the same sample. (c) A typical pump–probe trace obtained from a nanoplasmonic waveguide. (d) A typical pump–probe trace obtained from a photonic waveguide.

their performance. A SEM showing side-by-side nanoplasmonic and photonic waveguides is shown in Fig. 6(b). A typical trace obtained during the pump–probe experiments from a nanoplasmonic waveguide of length $L = 5.2$ μm and width $w = 95$ nm for a peak input power of $P_{peak} = 23.0$ W is shown in Fig. 6(c). Interference fringes become visible as the delay between the pump and probe pulses is decreased. The electric field amplitude in the nanoplasmonic waveguide reaches a maximum when the time delay between the two pulses is zero. A sharp drop in the signal transmission is visible at this point, signifying the presence of TPA and FCA. As free-carriers recombine, the FCA loss is reduced and a recovery tail is evident in the trace. A biexponential function is fit to this recovery tail and the resulting time constants are found to be $\tau_1 = 1.98 \pm 0.40$ ps and $\tau_2 = 17.9 \pm 6.8$ ps. Traces with distinct modulation depths and the same biexponential recovery tail were measured from waveguides with several lengths and larger widths of $w = 340$ nm.

Detailed physical investigation into these results has been presented in [4]. Briefly, after electron–hole pairs are excited via TPA, they are accelerated in the electric fields of the laser pulse. For sufficiently intense fields (~3 V/nm), electrons are ponderomotively accelerated to energies greater than the threshold for impact ionization ($E_{th} = 2.3$ eV [19]). In this way, a series of impact ionization collisions frees additional free-carriers, which are then accelerated in the laser field and undergo subsequent impact ionization collisions. Therefore the free-carriers are multiplied in an avalanche fashion, which enables strong modulation of the transmitted pulses over a very short length scale.

After the pulse excitation, the waveguide recovers from this interaction through two processes. The slower timescale arises from electron–hole recombination, where Au diffusion into the Si waveguide core creates recombination centers, enabling faster electron–hole recombination than bulk Si. The faster timescale represents electron sweeping in the intense field created by the femtosecond pulses. Tight, asymmetric fields close to the Au–Si interface cause cycle-by-cycle ponderomotive acceleration of conduction band electrons, imparting them with a velocity away from the Au–Si interface. Therefore, conduction band electrons are swept out of the probed region on an ultrafast timescale of ~2.0 ps, which is primarily determined by the saturation velocity of Si.

A pump–probe trace obtained from a photonic waveguide with length $L = 6.5$ μm and width $w = 340$ nm for a peak input power of $P_{peak} = 38.6$ W is shown in Fig. 6(d). Similar interference fringes are observed as the pump and probe pulses coincide in time. However, despite a longer interaction length and a higher peak input power, the modulation depth due to TPA and FCA is much less pronounced for the photonic waveguide. In addition, the recovery tale exhibits a single exponential trend with a much longer time constant $\tau = 378$ ps. In this case, free-carriers must diffuse to the waveguide sidewalls where a large density of partially bonded Si atoms give rise a continuous distribution of interface states through the energy bandgap. The absence of tightly confined nanoplasmonic fields significantly reduces the modulation efficiency and increases the recovery time of this device.

5. Conclusion

Nanoplasmonic waveguides with subwavelength cross-sectional dimensions were integrated onto a micron-scale characterization beam that allowed for characterization with macroscopic optical components. The structures were fabricated using two layers of EBL, creating masks for: (1) the lift-off and etching of Si-loaded nanoplasmonic waveguides, and (2) the definition of a characterization beam and a cleavage plane directly adjacent to the end-facets of the waveguides. The time-dynamics of the nonlinear loss mechanisms in the waveguide were characterized using a pump–probe delay line system, and it was found that the device recovered on two timescales, $\tau_1 = 1.98 \pm 0.40$ ps and $\tau_2 = 17.9 \pm 6.8$ ps, demonstrating potential device applications as subwavelength, ultrafast all-optical switches. By performing identical experiments on photonic waveguides, it was shown that the nanoplasmonic waveguide is superior in terms of modulation bandwidth and efficiency. The process steps used to fabricate these structures are compatible with typical semiconductor fabrication techniques. It is envisioned that this fabrication approach will be a valuable tool for accurate characterization of nonlinear nano-optical devices, and can easily accommodate a wide variety of device geometries.

Acknowledgement

This work was supported by the Natural Sciences and Engineering Research Council of Canada and by Alberta Innovates.

References

[1] R. Soref, IEEE J. Sel. Top. Quant. 12 (2006) 1678–1687.
[2] D.J. Dikken, M. Spasenovic, E. Verhagen, D. van Oosten, L. Kuipers, Opt. Express 18 (2010) 16112–16119.
[3] J. Homola, Chem. Rev. 108 (2008) 462–493.
[4] S. Sederberg, A.Y. Elezzabi, Phys. Rev. Lett. 113 (2014) 167401.
[5] S. Sederberg, A.Y. Elezzabi, Phys. Rev. Lett. 114 (2015) 227401.
[6] I. Fernandez-Cuesta, R.B. Nielsen, A. Boltasseva, X. Borrisé, F. Pérez-Murano, A. Kristensen, J. Vac. Sci. Technol., B 25 (2007) 2649–2653.
[7] M. Lu, L.E. Ocola, S.K. Gray, G.P. Wiederrecht, J. Vac. Sci. Technol., B 26 (2008) 2151–2155.
[8] C. Chiu, E. Lisicka-Skrzek, R.N. Tait, P. Berini, J. Vac. Sci. Technol., B 28 (2010) 729–735.
[9] C. Chiu, E. Lisicka-Skrzek, R.N. Tait, P. Berini, J. Vac. Sci. Technol., B 29 (2011) 062601.
[10] E. Kretschmann, Opt. Commun. 6 (1972) 185–187.
[11] S. Sederberg, V. Van, A.Y. Elezzabi, Appl. Phys. Lett. 96 (2010) 121101.
[12] R.H. Ritchie, E.T. Arakawa, J.J. Cowan, R.N. Hamm, Phys. Rev. Lett. 21 (1968) 1530–1533.
[13] J.-S. Huang, T. Feichtner, P. Biagioni, B. Hecht, Nano Lett. 9 (2009) 1897–1902.
[14] I.P. Radko, T. Holmgaard, Z. Han, K. Pedersen, S.I. Bozhevolnyi, Appl. Phys. Lett. 99 (2011) 213109.
[15] F. Marty, L. Rousseau, B. Saadany, B. Mercier, O. Français, Y. Mita, T. Bourouina, Microelectron. J. 36 (2005) 673–677.
[16] M.D. Henry, Ph.D. Thesis, ICP Etching of Silicon for Micro and Nanoscale Devices, 2010, pp. 51–52.
[17] J. Sanabia, K. Burcham, J. Klingfus, G. Piaszenski, M. Kahl, R. Jede, in: Conference on Lasers and Electro-Optics 2012, OSA Technical Digest, paper CM4L.3, 2012.
[18] R. Dekker, N. Usechak, M. Först, A. Driessen, J. Phys. D Appl. Phys. 40 (2007) R249–R271.
[19] P.A. Wolff, Phys. Rev. 95 (1954) 1415.